Supplementary Information

Coupling of dissolved organic carbon, sulfur and iron cycling in Black Sea sediments over the Holocene and the late Pleistocene: insights from an empirical dynamic model

Pei-Chuan Chuang[a,b*], Andrew W. Dale[b], Verena B. Heuer[a], Kai-Uwe Hinrichs[a], Matthias Zabel[a]

[a] MARUM – Center for Marine Environmental Sciences, University of Bremen, Leobener Str. 8, 28359 Bremen, Germany

[b] GEOMAR Helmholtz Centre for Ocean Research Kiel, Wischhofstr. 1–3, 24148 Kiel, Germany

*Correspondence to: Pei-Chuan Chuang (pchuang@geomar.de)

Reaction-transport model for site GeoB15105 in Black Sea

To investigate and quantify the processes controlling distributions of dissolved and particulate species in the upper 30 m of Black Sea sediments, the data from site Geo15105 were simulated with a transient diagenetic reaction-transport model. The model was based on previous diagenetic models by Burdige et al. (2016) and Egger et al. (2016) and expanded to simulate DOC cycling and its coupling to iron and sulfur turnover.

Four pools of reactive particulate organic matter (POC_i, i=1-4) undergoing remineralization at different rates in the sediments are assumed in the model. We considered four reactive and one refractory DOC fractions (DOC_i, i=1-4 and DOC_r) to link particulate organic carbon remineralization to DOC cycling (see main text). Fe oxides are separated into three pools depending on reactivity (i.e., Feoxα for highy reactive, Feoxβ for less reactive and Feoxγ for unreactive phases). Finally, the model simulates the distributions of 14 dissolved species (Cl^-, SO_4^{2-}, $\sum H_2S$, CH_4, NH_4^+, DIC, DOC_1, DOC_2, DOC_3, DOC_4, DOC_r, CH_3COO^-, Fe^{2+} and H_2) and 11 solid species (POC_1, POC_2, POC_3, POC_4, $Fe(OH)_3^{\alpha}$, $(Fe(OH)_3)^{\beta}$, $(Fe(OH)_3)^{\gamma}$, FeS, FeS_2, $FeCO_3$ and S^0). Biogeochemical reactions included are listed in Table S1. The sources and sinks of the model variables are listed in Table S2, and Table S3 provides the model parameters.

Vertical depth profiles of the dissolved and solid species were simulated using 1-D mass conservation equations (Berner, 1980; Boudreau, 1997):

$$\varphi(x) \cdot \frac{\partial C_i(x,t)}{\partial t} = \frac{\partial\left(\varphi(x) \cdot D_S(x) \cdot \frac{\partial C_i(x,t)}{\partial x}\right)}{\partial x} - \frac{\partial\left(\varphi(x) \cdot v(x) \cdot C_i(x,t)\right)}{\partial x} + \varphi(x) \cdot \Sigma R_{C_i}(x,t) \qquad \text{(Eq. S1)}$$

$$(1-\varphi(x)) \cdot \frac{\partial G_j(x,t)}{\partial t} = -\frac{\partial\left((1-\varphi(x)) \cdot w(x) \cdot G_j(x,t)\right)}{\partial x} + (1-\varphi(x)) \cdot \Sigma R_{G_j}(x,t) \qquad \text{(Eq. S2)}$$

where x (cm) is sediment depth, t (yr) is time, φ is porosity, D_S (cm^2 yr^{-1}) is the solute–specific diffusion coefficient in the sediment, C_i (μmol cm^{-3} of porewater) is the concentration of solute i, G_j is the content of solid species j (dry weight percent, wt.%), v (cm yr^{-1}) is the net velocity of solutes by burial and compaction in addition to upward fluid flow imposed at the lower boundary of the model, w (cm yr^{-1}) is the burial velocity of solids and ΣR_{C_i} and ΣR_{G_j} are the sum of biogeochemical reactions for dissolved and solid species (Table S2).

Sediment porosity in the model decreases with depth:

$$\varphi(x) = \varphi_f + \left(\varphi_0 - \varphi_f\right) e^{-px} \qquad \text{(Eq. S3)}$$

Parameterization of this function was made based on measured data at site GeoB15105 (Fig. 3).

The velocity of interstitial fluids and solids was calculated as (see main text):

$$v(x) = \frac{\varphi_f \cdot w_f - v_0 \cdot \varphi_0}{\varphi(x)} \quad \text{(Eq. S4)}$$

$$w(x) = \frac{\left(1-\varphi_f\right) \cdot w_f}{\left(1-\varphi(x)\right)} \quad \text{(Eq. S5)}$$

$$\text{where } w_f = \frac{x_{\mathrm{RF2}}}{age_{\mathrm{RF2}}} + \frac{\left(\varphi_f-\varphi_0\right) \cdot \left(e^{-p \cdot x_{\mathrm{RF2}}}-1\right)}{p \cdot age_{\mathrm{RF2}} \cdot \left(\varphi_f-1\right)} \quad \text{(Eq. S6)}$$

The sediment burial velocity in compacted sediments (w_f) was determined from the known age of the sediment layers at reaction front #2 (age_{RF2} = 7995 yr BP). The resulting sedimentation velocity was 23.3 cm kyr^{-1}, which fits with the chronology of nearby sites (MD MD04-2760 and MD04-2788) (Kwiecien et al., 2008). Burial results in the downward movement of both sediment particles and porewater relative to the sediment water interface. Externally impressed fluid flow (v_0) transports solutes upwards. The net direction of travel depends on the relative magnitude of the terms in the numerator in Eq. (S4). For site GeoB15105, $v_0 \cdot \varphi_0 > \varphi_f \cdot w_f$ and advection transports solutes upwards.

The free-solution diffusion coefficient of each solute in seawater ($D_M(x)$) was corrected for tortuosity using the modified Weissberg equation (Boudreau, 1997) to give the diffusion coefficient in the sediment ($D_S(x)$):

$$D_S(x) = \frac{D_M}{1-2\ln\varphi(x)} \quad \text{(Eq. S7)}$$

D_M was calculated for in situ temperature, salinity and pressure (Boudreau, 1997).

POC degradation was constrained by DOC, acetate, sulfate, DIC and ammonium data. Other microbially mediated mineralization processes such as aerobic respiration, denitrification, dissimilatory manganese reduction were ignored, since their quantitative significance on formation of methane is expected to be minor in these deep water anoxic sediments (water depth = 1268m) (Zabel et al., 2012). Since the iron (oxyhydr)oxides content is used as the upper boundary condition, the reaction between oxygen (O_2) and Fe^{2+} is implicitly accounted for aerobic oxidation of ammonium and hydrogen sulfide, typically in the upper mm or cm of the sediment, were ignored since these processes were expected to make little difference to concentrations extended over several meters of sediment.

Time-dependent boundary conditions at the sediment surface were applied for Cl^-, SO_4^{2-}, DIC and $\sum H_2S$ and solid species except S^0 (Fig. 2). The upper boundary conditions of Cl^- and SO_4^{2-} were

converted from the transient evolution of salinity assuming an initial salinity of 1 for the freshwater lake and a linear increase to a salinity of 22 between 9300 and 2000 yr BP (Bahr et al., 2008; Soulet et al., 2010). The transient evolution of DIC was applied to the upper boundary by using an initial DIC concentration of 0.6 mM for the freshwater lake and a linear increase to the measured DIC concentration of 5.25 mM at sediment surface between 9300 and 2000 yr BP. The initial DIC concentration of 0.6 mM was calculated from the ratio between DIC and Cl^- in modern ocean and the initial concentration of Cl^-. Best results were obtained by applying measured bottom water $\sum H_2S$ concentrations (Fig. 2c) of 0.9 mM to the upper boundary after 1500 yr BP, coincident with the establishment of modern salinity levels (Soulet et al., 2010). Simulation results with high bottom water sulfide levels prior to this were unsatisfactory, and previous work suggests that bottom water $\sum H_2S$ may been < 0.1 mM at this time (Egger et al., 2016). The age of each measured solid species at each depth (age(x)) and its content were initially applied as time-dependent upper boundary conditions using Eq. 7 in the main manuscript. These were then fine-tuned to provide optimal fits to the entire suit of measured biogeochemical profiles (Fig. 3).

Constant concentrations for remaining solutes and a fixed S^0 content were imposed at the upper boundary (Table S4). The model was solved with a zero-gradient condition for all dissolved and solid species except CH_4 at the lower boundary (Table S4). A fixed concentration obtained was used for CH_4 at the lower boundary that was adjusted to fit the CH_4 data. The observation of gas bubbles and gas hydrates in the nearby sediments suggests that CH_4 reaches solubility with bubbles and/or hydrates in situ (Bohrmann et al., 2011; Minshull et al., 2020). The spatial derivatives of the coupled partial differential equations were approximated using finite differences and solved using the method-of-lines (Boudreau, 1997) using the ordinary differential equation solver (NDSolve) in MATHEMATICA v. 10.0. All simulations were spun-up to steady state to achieve zero gradients (except CH_4) at the lower boundary using a grid spacing which increased from 0.01 cm at the sediment surface to 10.93 cm at depth (see main text).

Table S1: Reaction network used in the model.

Reaction and stoichiometry (Carbon transformation from POC to DOC and then to DIC or acetate)	Kinetic rate law [a]	Reaction number
<u>POC degradation and DOC production</u>: $CH_2O(NH_3)_{r_{N(s)}} + r_N H^+ \rightarrow CH_2O_{(aq)} + r_N \cdot NH_4^+$	$R_{POC_i deg} = k_{POC_i} \cdot POC_i$ (i=1-4)	R1
	$R_{DOC_i p} = (1 - a_i) \cdot f_C \cdot R_{POC_i deg}$ (i=1-4)	R2
	$R_{DOC_r p} = \sum_{i=1}^{4} a_i \cdot f_C \cdot R_{POC_i deg}$	R3
<u>DOC degradation and DIC/H_2 or acetate production</u>: $CH_2O_{(aq)} + 2f_{ferm} \cdot H_2O \rightarrow f_{ferm} \cdot HCO_3^- + 2f_{ferm} \cdot H_2 + \frac{(1 - f_{ferm})}{2} \cdot CH_3COO^- + \frac{(1 + f_{ferm})}{2} \cdot H^+$	$R_{DOC_i deg} = k_{DOC_i} \cdot DOC_i$ (i=1-4)	R4
	$R_{DOC_r deg} = k_{DOC_r} \cdot DOC_r$	R5
	$R_{hyDOC deg} = \sum_{i=1}^{4} R_{DOC_i deg} \cdot f_{ferm_i} + R_{DOC_r deg} \cdot f_{ferm_r}$	R6
	$R_{acDOC deg} = \sum_{i=1}^{4} R_{DOC_i deg} \cdot \frac{(1 - f_{ferm_i})}{2} + R_{DOC_r deg} \cdot \frac{(1 - f_{ferm_r})}{2}$	R7

Table S1(Continued): Reaction network used in the model.

Reaction and stoichiometry (Primary redox reactions)	Kinetic rate law [a]	Reaction number
DOC oxidation coupled to iron reduction (hydrogenotrophic iron reduction): $CH_2O_{(aq)} + 4Fe(OH)_3^{\alpha} + 7H^+ \rightarrow 4Fe^{2+} + HCO_3^- + 10H_2O$	$R_{hyFeR} = 4 \cdot R_{hyDOCdeg} \cdot \frac{Fe(OH)_3^{\alpha}}{K_{hyFeR} + Fe(OH)_3^{\alpha}}$	R8
DOC oxidation coupled to sulfate reduction (hydrogenotrophic sulfate reduction): $CH_2O_{(aq)} + 0.5\,SO_4^{2-} \rightarrow HCO_3^- + 0.5H^+ + 0.5HS^-$	$R_{hySR} = 0.5 \cdot R_{hyDOCdeg} \cdot \frac{SO_4^{2-}}{K_{hySR} + SO_4^{2-}} \cdot \frac{K_{hyFeR}}{K_{hyFeR} + Fe(OH)_3^{\alpha}}$	R9
DOC oxidation coupled to methanogenesis (hydrogenotrophic methanogenesis): $CH_2O_{(aq)} + 0.5H_2O \rightarrow 0.5CH_4 + 0.5HCO_3^- + 0.5H^+$	$R_{hyME} = 0.5 \cdot R_{hyDOCdeg} \cdot \frac{K_{hySR}}{K_{hySR} + SO_4^{2-}} \cdot \frac{K_{hyFeR}}{K_{hyFeR} + Fe(OH)_3^{\alpha}}$	R10
DOC oxidation coupled to iron reduction (acetoclastic iron reduction): $CH_3COO^- + 8Fe(OH)_3^{\alpha} + 15H^+ \rightarrow 8Fe^{2+} + 2HCO_3^- + 20H_2O$	$R_{acFeR} = k_{acFeR} \cdot CH_3COO^- \cdot \frac{Fe(OH)_3^{\alpha}}{K_{acFeR} + Fe(OH)_3^{\alpha}}$	R11
DOC oxidation coupled to sulfate reduction (acetoclastic sulfate reduction): $SO_4^{2-} + CH_3COO^- \rightarrow HS^- + 2HCO_3^-$	$R_{acSR} = k_{acSR} \cdot CH_3COO^- \cdot \frac{SO_4^{2-}}{K_{acSR} + SO_4^{2-}} \cdot \frac{K_{acFeR}}{K_{acFeR} + Fe(OH)_3^{\alpha}}$	R12
DOC oxidation coupled to methanogenesis (acetoclastic methanogenesis): $CH_3COO^- + H_2O \rightarrow CH_4 + HCO_3^-$	$R_{acME} = k_{acME} \cdot CH_3COO^- \cdot \frac{K_{acSR}}{K_{acSR} + SO_4^{2-}} \cdot \frac{K_{acFeR}}{K_{acFeR} + Fe(OH)_3^{\alpha}}$	R13

Table S1(Continued): Reaction network used in the model.

Reaction and stoichiometry (Secondary redox and other reactions)	Kinetic rate law [a]	No. of reactions
Ammonium released from POC degradation: $CH_2O(NH_3)_{r_{N(s)}} + r_N H^+ \rightarrow CH_2O_{(aq)} + r_N \cdot NH_4^+$	$R_{AMF} = \sum_{i=1}^{4} rN \cdot R_{POC_i deg} \cdot f_C$	R14
Anaerobic methane oxidation with sulfate: $CH_4 + SO_4^{2-} \rightarrow HS^- + HCO_3^- + H_2O$	$R_{SO4CH4} = k_{SO4CH4} \cdot SO_4^{2-} \cdot \frac{CH_4}{K_{CH_4AOM} + CH_4}$	R15
$Fe(OH)_3^{\alpha}$ reduction by $\sum H_2S$: $2Fe(OH)_3^{\alpha} + 5H^+ + HS^- \rightarrow 2Fe^{2+} + S^0 + 6H_2O$	$R_{FeoxαH2S} = k_{FeoxαH2S} \cdot Fe(OH)_3^{\alpha} \cdot f_{Fe} \cdot HS^-$	R16
$Fe(OH)_3^{\beta}$ reduction by $\sum H_2S$: $2Fe(OH)_3^{\beta} + 5H^+ + HS^- \rightarrow 2Fe^{2+} + S^0 + 6H_2O$	$R_{FeoxβH2S} = k_{FeoxβH2S} \cdot Fe(OH)_3^{\beta} \cdot f_{Fe} \cdot HS^-$	R17
FeS precipitation: $Fe^{2+} + HS^- \rightarrow FeS + H^+$	$R_{Fe2H2S} = k_{Fe2H2S} \cdot Fe^{2+} \cdot HS^-$	R18
FeS_2 precipitation (H_2S pathway): $FeS + HS^- + H^+ \rightarrow FeS_2 + H_2$	$R_{FeSH2S} = k_{FeSH2S} \cdot FeS \cdot f_{Fe} \cdot HS^-$	R19
S^0 disproportionation: $4S^0 + 4H_2O \rightarrow 3HS^- + 5H^+ + SO_4^{2-}$	$R_{S0} = k_{S0} \cdot S^0 \cdot f_S$	R20
FeS_2 precipitation (polysulfide pathway): $FeS + S^0 \rightarrow FeS_2$	$R_{FeSS0} = k_{FeSS0} \cdot FeS \cdot f_{Fe} \cdot S^0 \cdot f_S$	R21
Anaerobic methane oxidation with $Fe(OH)_3^{\alpha}$: $8Fe(OH)_3^{\alpha} + CH_4 + 15H^+ \rightarrow HCO_3^- + 8Fe^{2+} + 21H_2O$	$R_{FeoxαCH4} = k_{FeoxαCH4} \cdot Fe(OH)_3^{\alpha} \cdot f_{Fe} \cdot CH_4$	R22
Anaerobic methane oxidation with $Fe(OH)_3^{\beta}$: $8Fe(OH)_3^{\beta} + CH_4 + 15H^+ \rightarrow HCO_3^- + 8Fe^{2+} + 21H_2O$	$R_{FeoxβCH4} = k_{FeoxβCH4} \cdot Fe(OH)_3^{\beta} \cdot f_{Fe} \cdot CH_4$	R23
$Fe(OH)_3^{\beta}$ recrystallized from $Fe(OH)_3^{\alpha}$: $Fe(OH)_3^{\alpha} \rightarrow Fe(OH)_3^{\beta}$	$R_{FeoxαFeoxβ} = k_{FeoxαFeoxβ} \cdot Fe(OH)_3^{\alpha} \cdot f_{Fe}$	R24
$Fe(OH)_3^{\gamma}$ recrystallized from $Fe(OH)_3^{\beta}$: $Fe(OH)_3^{\beta} \rightarrow Fe(OH)_3^{\gamma}$	$R_{FeoxβFeoxγ} = k_{FeoxβFeoxγ} \cdot Fe(OH)_3^{\beta} \cdot f_{Fe}$	R25
Siderite precipitation: $Fe^{2+} + 2HCO_3^- \rightarrow FeCO_3 + 2H^+$	$R_{FeDIC} = k_{FeDIC} \cdot Fe^{2+} \cdot DIC$	R26
Siderite conversion to FeS: $FeCO_3 + HS^- \rightarrow FeS + HCO_3^-$	$R_{FeCO3H2S} = k_{FeCO3H2S} \cdot FeCO_3 \cdot f_{Fe} \cdot HS^-$	R27
Carbonate reduction: $HCO_3^- + 4H_2 + H^+ \rightarrow CH_4 + 3H_2O$	$R_{DICH2} = k_{DICH2} \cdot DIC \cdot H_2$	R28

[a] The factors, f ($f_C = \frac{ds \times (1-\Phi) \times 10^4}{MW_C \times \varphi}$, $f_{Fe} = \frac{ds \times (1-\Phi) \times 10^4}{MW_{Fe} \times \varphi}$, $f_S = \frac{ds \times (1-\Phi) \times 10^4}{MW_S \times \varphi}$), are used to convert between solid and dissolved species concentrations, where MW_C is the molecular weight of carbon (12 g mol^{-1}), MW_{Fe} is the molecular weight of iron (55.8 g mol^{-1}) and MW_S is the molecular weight of sulfur (32 g mol^{-1}). Other parameters are described in Table S3.

Table S2: Mass balance of model variables.

Modeled species	Rates
Dissolved species	
Cl^-	0
SO_4^{2-}	$-R_{\mathrm{hySR}}-R_{\mathrm{SO4CH4}} - R_{\mathrm{acSR}} + R_{\mathrm{S0}}$
$\sum H_2S$	$+R_{\mathrm{hySR}}+R_{\mathrm{SO4CH4}} + R_{\mathrm{acSR}} - (R_{\mathrm{FeoxαH2S}} + R_{\mathrm{FeoxβH2S}}) - R_{\mathrm{Fe2H2S}} - R_{\mathrm{FeSH2S}} + 3 \cdot R_{\mathrm{S0}} - R_{\mathrm{FeCO3H2S}}$
CH_4	$+R_{\mathrm{hyME}}-R_{\mathrm{SO4CH4}} + R_{\mathrm{acME}} - (R_{\mathrm{FeoxαCH4}} + R_{\mathrm{FeoxβCH4}}) + 0.25 \cdot R_{\mathrm{DICH2}}$
NH_4^+	R_{AMF}
DIC	$2 \cdot R_{\mathrm{hySR}} + R_{\mathrm{hyME}}+R_{\mathrm{SO4CH4}} + 2 \cdot R_{\mathrm{acSR}} + R_{\mathrm{acME}} + (R_{\mathrm{FeoxαCH4}} + R_{\mathrm{FeoxβCH4}}) - R_{\mathrm{FeDIC}} + R_{\mathrm{FeCO3H2S}} + 0.25 \cdot R_{\mathrm{hyFeR}} + 2 \cdot R_{\mathrm{acFeR}} - 0.25 \cdot R_{\mathrm{DICH2}}$
DOC_i	$R_{\mathrm{DOC_ip}} - R_{\mathrm{DOC_ideg}}$ (i=1-4)
DOC_r	$R_{\mathrm{DOC_rp}} - R_{\mathrm{DOC_rdeg}}$
CH_3COO^-	$+R_{\mathrm{acDOCdeg}} - R_{\mathrm{acSR}} - R_{\mathrm{acME}}-R_{\mathrm{acFeR}}$
Fe^{2+}	$+2 \cdot (R_{\mathrm{FeoxαH2S}} + R_{\mathrm{FeoxβH2S}}) - R_{\mathrm{Fe2H2S}} + 8 \cdot (R_{\mathrm{FeoxαCH4}} + R_{\mathrm{FeoxβCH4}}) - R_{\mathrm{FeDIC}} + R_{\mathrm{hyFeR}} + 8 \cdot R_{\mathrm{acFeR}}$
H_2	$+R_{\mathrm{FeSH2S}} - R_{\mathrm{DICH2}}$
Solid species	
POC_i	$-R_{\mathrm{POC_ideg}}$ (i=1-4)
$Fe(OH)_3^{\alpha}$	$\frac{-2 \cdot R_{\mathrm{FeoxαH2S}} - 8 \cdot R_{\mathrm{FeoxαCH4}} - R_{\mathrm{FeoxαFeoxβ}} - R_{\mathrm{hyFeR}} - 8 \cdot R_{\mathrm{acFeR}}}{f_{\mathrm{Fe}}}$
$Fe(OH)_3^{\beta}$	$\frac{-2 \cdot R_{\mathrm{FeoxβH2S}} - 8 \cdot R_{\mathrm{FeoxβCH4}} + R_{\mathrm{FeoxαFeoxβ}} - R_{\mathrm{FeoxβFeoxγ}}}{f_{\mathrm{Fe}}}$
$Fe(OH)_3^{\gamma}$	$\frac{+R_{\mathrm{FeoxβFeoxγ}}}{f_{\mathrm{Fe}}}$
FeS	$\frac{+R_{\mathrm{Fe2H2S}} - R_{\mathrm{FeSH2S}} - R_{\mathrm{FeSS0}} + R_{\mathrm{FeCO3H2S}}}{f_{\mathrm{Fe}}}$
FeS_2	$\frac{+R_{\mathrm{FeSH2S}} + R_{\mathrm{FeSS0}}}{f_{\mathrm{Fe}}}$
$FeCO_3$	$\frac{+R_{FeDIC} - R_{FeCO3HS}}{f_{\mathrm{Fe}}}$
S^0	$\frac{+(R_{FeoxαHS} + R_{FeoxβHS}) - 4 \cdot R_{S0} - R_{FeSS0}}{f_{\mathrm{S}}}$

Table S3: Imposed and best-fit parameters for site GeoB15105

Parameter	Description	Baseline	Unit	Source
T	Bottom water temperature	282.15	K	M
L	Length of sediment column	3000	cm	C
S	Bottom water salinity	22	-	M
d_s	Dry sediment density	2.31	g cm^{-3}	L
d_{sw}	Seawater density	1.033	g cm^{-3}	L
w_f	Burial velocity of compacted sediment	0.023	cm yr^{-1}	C
x_{RF2}	Depth of the boundary between Unit II/III	417	cm	M
age_{RF2}	Calibrated ^{14}C age of the boundary between Unit II/III	7995	yr	L[1,2]
P	Pressure at seafloor	129	bar	M
v_0	Upward fluid velocity	0.13	cm yr^{-1}	C
φ_0	Sediment porosity at zero depth	0.95	-	M
φ_f	Sediment porosity at infinite depth	0.5	-	M
p	Depth attenuation coefficient of porosity	1/395	cm^{-1}	C
D_{SO_4}	Diffusion coefficient for SO_4^{2-}	220	cm^2 yr^{-1}	L[3]
D_{CH_4}	Diffusion coefficient for CH_4	343	cm^2 yr^{-1}	L[3]
D_{NH_4}	Diffusion coefficient for NH_4^+	417	cm^2 yr^{-1}	L[3]
D_{DIC}	Diffusion coefficient for DIC	238	cm^2 yr^{-1}	L[3]
$D_{\sum H_2S}$	Diffusion coefficient for $\sum H_2S$	382	cm^2 yr^{-1}	L[3]
D_{Cl}	Diffusion coefficient for Cl^-	335	cm^2 yr^{-1}	L[3]
D_{DOC}	Diffusion coefficient for $DOC_{i,\ i=1-4}$, DOC_r	50	cm^2 yr^{-1}	L[4]
$D_{CH_3COO^-}$	Diffusion coefficient for CH_3COO^-	221	cm^2 yr^{-1}	L[3]
$D_{Fe^{2+}}$	Diffusion coefficient for Fe^{2+}	147	cm^2 yr^{-1}	L[3]
D_{H_2}	Diffusion coefficient for H_2	605	cm^2 yr^{-1}	L[6]
k_{POC_1}	First order rate constant for POC_1 degradation	4×10^{-4}	yr^{-1}	C
k_{POC_2}	First order rate constant for POC_2 degradation	1.72×10^{-5}	yr^{-1}	C
k_{POC_3}	First order rate constant for POC_3 degradation	3.27×10^{-7}	yr^{-1}	C
k_{POC_4}	First order rate constant for POC_4 degradation	5.04×10^{-8}	yr^{-1}	C
a_1	Fraction of POC_1 degradation that produces refractory DOC_r	1%	-	C
a_2	Fraction of POC_2 degradation that produces refractory DOC_r	2%	-	C
a_3	Fraction of POC_3 degradation that produces refractory DOC_r	2.07%	-	C
a_4	Fraction of POC_4 degradation that produces refractory DOC_r	0.78%	-	C
f_{ferm_1}	Fraction of DOC_1 degradation that produces DIC/H_2	100%	-	C
f_{ferm_2}	Fraction of DOC_2 degradation that produces DIC/H_2	10%	-	C
f_{ferm_3}	Fraction of DOC_3 degradation that produces DIC/H_2	0	-	C
f_{ferm_4}	Fraction of DOC_4 degradation that produces DIC/H_2	0	-	C
f_{ferm_r}	Fraction of DOC_r degradation that produces DIC/H_2	20%	-	C
k_{DOC_1}	First order rate constant for the degradation of DOC_1	35.88	yr^{-1}	C
k_{DOC_2}	First order rate constant for the degradation of DOC_2	1.00×10^{-2}	yr^{-1}	C
k_{DOC_3}	First order rate constant for the degradation of DOC_3	1.02×10^{-4}	yr^{-1}	C
k_{DOC_4}	First order rate constant for the degradation of DOC_4	1.36×10^{-5}	yr^{-1}	C
k_{DOC_r}	First order rate constant for the degradation of DOC_r	5.10×10^{-7}	yr^{-1}	C
K_{hyFeR}	Limiting concentration of Feox for hydrogenotrophic iron reduction	0.5	Fe g/g	C
K_{hySR}	Limiting concentration of SO_4^{2-} for hydrogenotrophic sulfate reduction	1	mM	C
K_{acFeR}	Limiting concentration of Feox for acetoclastic iron reduction	0.5	Fe g/g	C
K_{acSR}	Limiting concentration of SO_4^{2-} for acetoclastic sulfate reduction	1	mM	C
K_{CH_4AOM}	Limiting concentration of CH_4 for anaerobic methane oxidation with sulfate	0.001	mM	C
rN	N:C mineralization ratio of POC_i i=1-4	1:8	-	C
k_{acFeR}	Kinetic constant for R_{acFeR}	0.014	yr^{-1}	C
k_{acSR}	Kinetic constant for R_{acSR}	0.131	yr^{-1}	C
k_{acME}	Kinetic constant for R_{acME}	0.036	yr^{-1}	C
k_{SO4CH4}	Kinetic constant for R_{SO4CH4}	1.16×10^{-4}	mM^{-1} yr^{-1}	C
$k_{FeoxαH2S}$	Kinetic constant for $R_{FeoxαH2S}$	38	mM^{-1} yr^{-1}	C
$k_{FeoxβH2S}$	Kinetic constant for $R_{FeoxβH2S}$	34.5	mM^{-1} yr^{-1}	C
k_{Fe2H2S}	Kinetic constant for R_{Fe2H2S}	9.375	mM^{-1} yr^{-1}	C
k_{FeSH2S}	Kinetic constant for R_{FeSH2S}	0.012	mM^{-1} yr^{-1}	C
k_{S0}	Kinetic constant for R_{S0}	3	yr^{-1}	L[5]
k_{FeSS0}	Kinetic constant for R_{FeSS0}	1	mM^{-1} yr^{-1}	L[5]
$k_{FeoxαCH4}$	Kinetic constant for $R_{FeoxαCH4}$	4.0×10^{-9}	mM^{-1} yr^{-1}	C
$k_{FeoxβCH4}$	Kinetic constant for $R_{FeoxβCH4}$	2.5×10^{-10}	mM^{-1} yr^{-1}	C
$k_{FeoxαFeoxβ}$	Kinetic constant for $R_{FeoxαFeoxβ}$	0.6	yr^{-1}	L[5]
$k_{FeoxβFeoxγ}$	Kinetic constant for $R_{FeoxβFeoxγ}$	2.6×10^{-5}	yr^{-1}	C
k_{FeDIC}	Kinetic constant for R_{FeDIC}	1.62×10^{-4}	mM^{-1} yr^{-1}	C

k_{FeCO3H2S}	Kinetic constant for R_{FeCO3H2S}	1.33×10^{-4}	$mM^{-1}\ yr^{-1}$	C
k_{DICH2}	Kinetic constant for R_{DICH2}	1×10^{6}	$mM^{-1}\ yr^{-1}$	C

[a] Parameter values were based on the following sources: C. Constrained with the model. M. Measured. L. Assumed value from literature: [1]Lamy et al. (2006); [2]Kwiecien et al. (2006); [3]Boudreau (1997); [4]Burdige et al. (2016); [5]Egger et al. (2016); [6]Schulz, 2000.

Table S4: Model boundary conditions for site GeoB15105

Variable	Surface[a]	Unit	Bottom	Unit
Cl^-	$Cl^-(t)$	mM	$\partial Cl^- / \partial x = 0$	mM/cm
SO_4^{2-}	$SO_4^{2-}(t)$	mM	$\partial SO_4^{2-} / \partial x = 0$	mM/cm
$\sum H_2S$	$\sum H_2S\,(t)$	mM	$\partial \sum H_2S / \partial x = 0$	mM/cm
CH_4	0	mM	60	mM
NH_4^+	0.1106	mM	$\partial NH_4^+ / \partial x = 0$	mM/cm
DIC	DIC(t)	nM	$\partial DIC / \partial x = 0$	mM/cm
DOC_1	0	mM	$\partial DOC_1 / \partial x = 0$	mM/cm
DOC_2	0	mM	$\partial DOC_2 / \partial x = 0$	mM/cm
DOC_3	0	mM	$\partial DOC_3 / \partial x = 0$	mM/cm
DOC_4	0	mM	$\partial DOC_4 / \partial x = 0$	mM/cm
DOC_r	2.6	mM	$\partial DOC_r / \partial x = 0$	mM/cm
CH_3COO^-	0	mM	$\partial CH_3COO^- / \partial x = 0$	mM/cm
Fe^{2+}	0	mM	$\partial Fe^{2+} / \partial x = 0$	mM/cm
H_2	0	mM	$\partial H_2 / \partial x = 0$	mM/cm
POC_1	$POC_1(t)$	wt.%	$\partial POC_1 / \partial x = 0$	wt.%/cm
POC_2	$POC_2(t)$	wt.%	$\partial POC_2 / \partial x = 0$	wt.%/cm
POC_3	$POC_3(t)$	wt.%	$\partial POC_3 / \partial x = 0$	wt.%/cm
POC_4	$POC_4(t)$	wt.%	$\partial POC_4 / \partial x = 0$	wt.%/cm
$Fe(OH)_3^{\alpha}$	$Fe(OH)_3^{\alpha}(t)$	wt.%	$\partial Fe(OH)_3^{\alpha} / \partial x = 0$	wt.%/cm
$(Fe(OH)_3)^{\beta}$	$(Fe(OH)_3)^{\beta}(t)$	wt.%	$\partial (Fe(OH)_3)^{\beta} / \partial x = 0$	wt.%/cm
$(Fe(OH)_3)^{\gamma}$	$(Fe(OH)_3)^{\gamma}(t)$	wt.%	$\partial (Fe(OH)_3)^{\gamma} / \partial x = 0$	wt.%/cm
FeS	$FeS(t)$	wt.%	$\partial FeS / \partial x = 0$	wt.%/cm
FeS_2	$FeS_2(t)$	wt.%	$\partial FeS_2 / \partial x = 0$	wt.%/cm
$FeCO_3$	$FeCO_3(t)$	wt.%	$\partial FeCO_3 / \partial x = 0$	wt.%/cm
S^0	0	wt.%	$\partial S_0 / \partial x = 0$	wt.%/cm

[a] $Cl^-(t)$ and $SO_4^{2-}(t)$ concentrations are the function of salinity (Fig. 2) $\left(Cl^-(t) = \frac{salinity(t)\times 10^3}{1.80655 \cdot MW_{Cl} \cdot dsw}; SO_4^{2-}(t) = \frac{salinity(t)\times 10^3}{1.80655 \cdot MW_{SO_4^{2-}} \cdot dsw}\right)$. For other time-dependent boundary conditions, see Fig. 2 in main text.

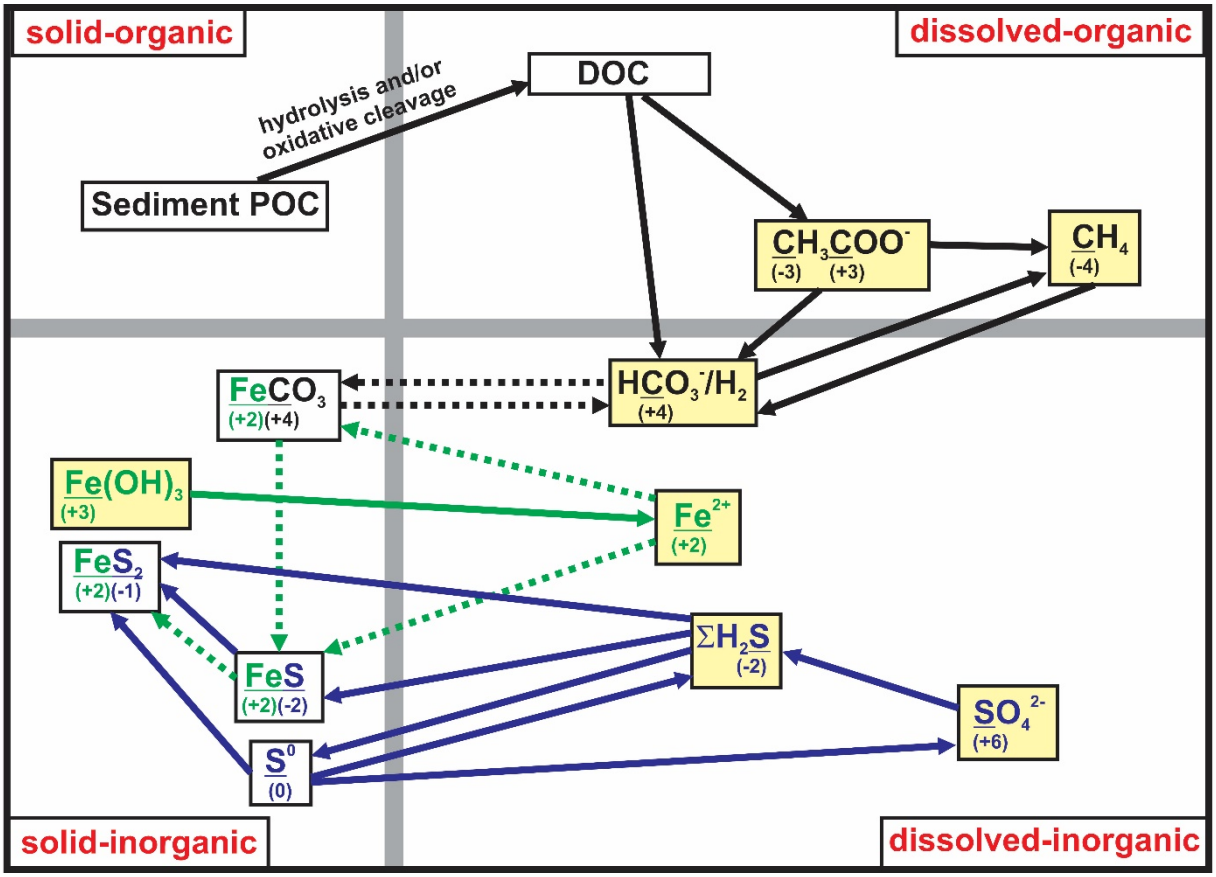

Fig. S1: Schematic representation of the reaction-transport model for interactions between organic carbon, inorganic carbon, sulfur and iron species in the solid and dissolved phases which link the primary and secondary redox reactions and other chemical reactions under non-steady state conditions. The number below the underlined element is the oxidation state. Elements undergoing a change in oxidation state are represented by solid arrows and those with no change by dashed arrows. The figure builds on the conceptual models of Burdige et al. (2016) and Egger et al. (2016). Note that only one intermediate DOC step is included in our model.

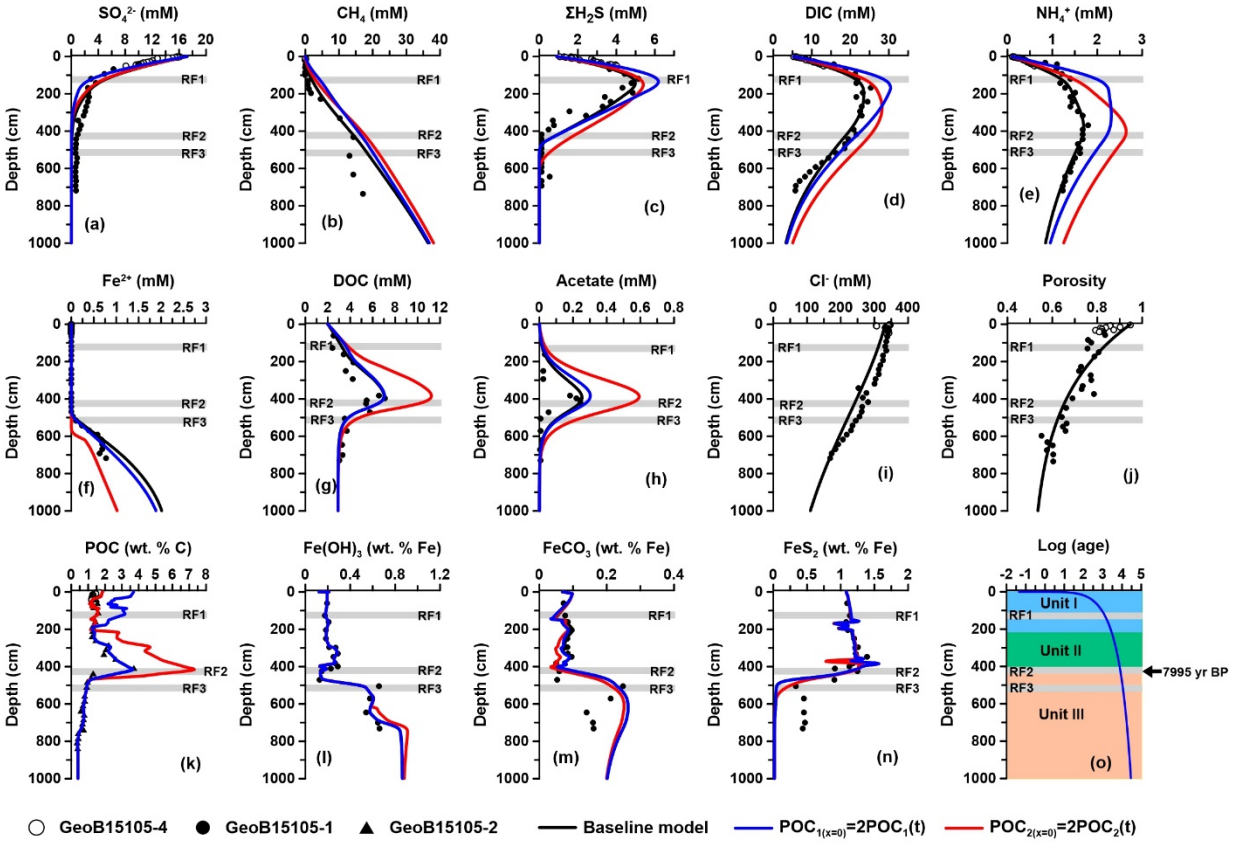

Fig. S2: Model sensitivity analysis of POC_1 and POC_2 content at the upper boundary at site GeoB15105. Baseline values are shown in black curves and measured data as symbols. The gray bars represent the depths of three reaction fronts. The simulated profiles are extracted from the last simulation year. The results show that POC_1 and POC_2 inputs and reactivity are the main driving forces for the redox reactions at RF1 and RF2, respectively.

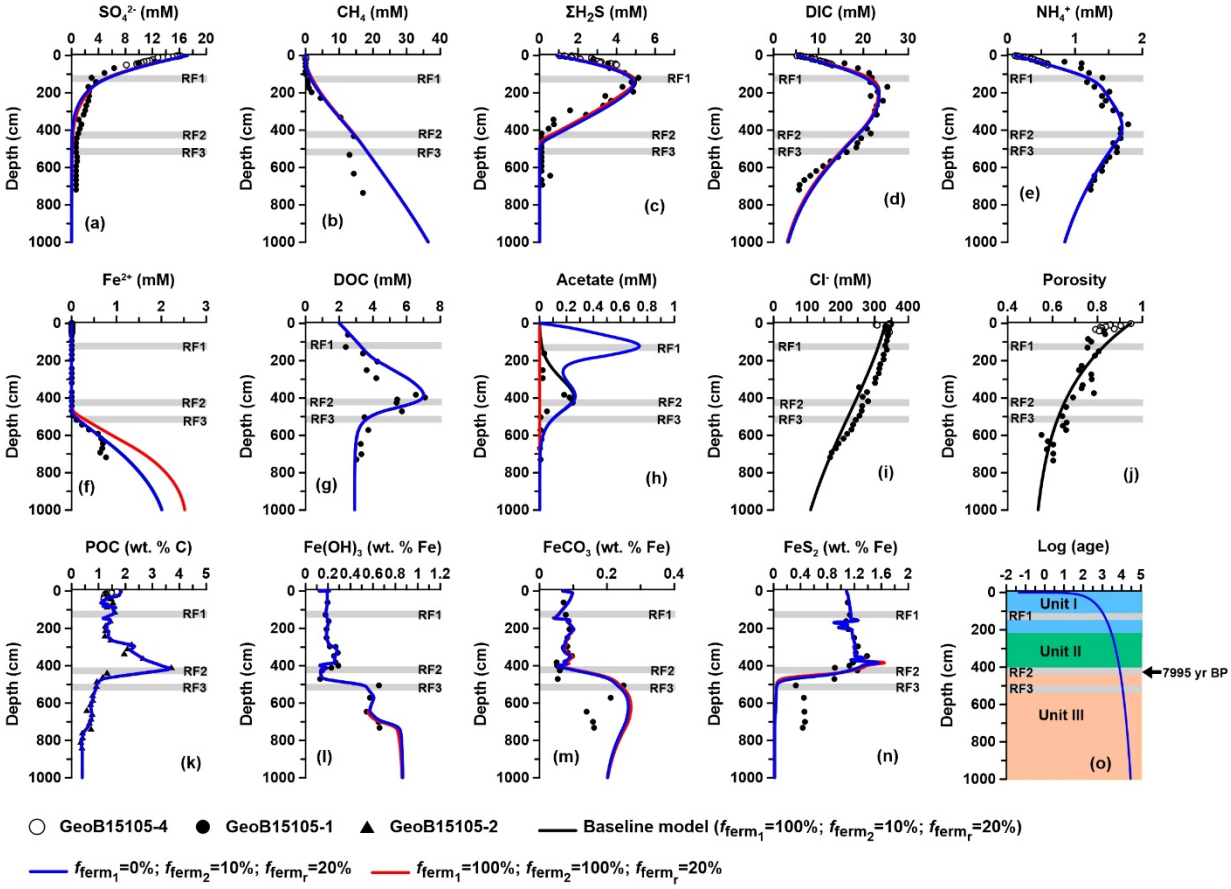

Fig. S3: Model sensitivity analysis of DOC_1 and DOC_2 degradation producing DIC/H_2 (R6) and acetate (R7) at site GeoB15105. Baseline values are shown in black curves and measured data as symbols. The gray bars represent the depths of three reaction fronts. The simulated profiles are extracted from the last simulation year. The results show that DOC_2 is the main source of acetate rather than DOC_1.

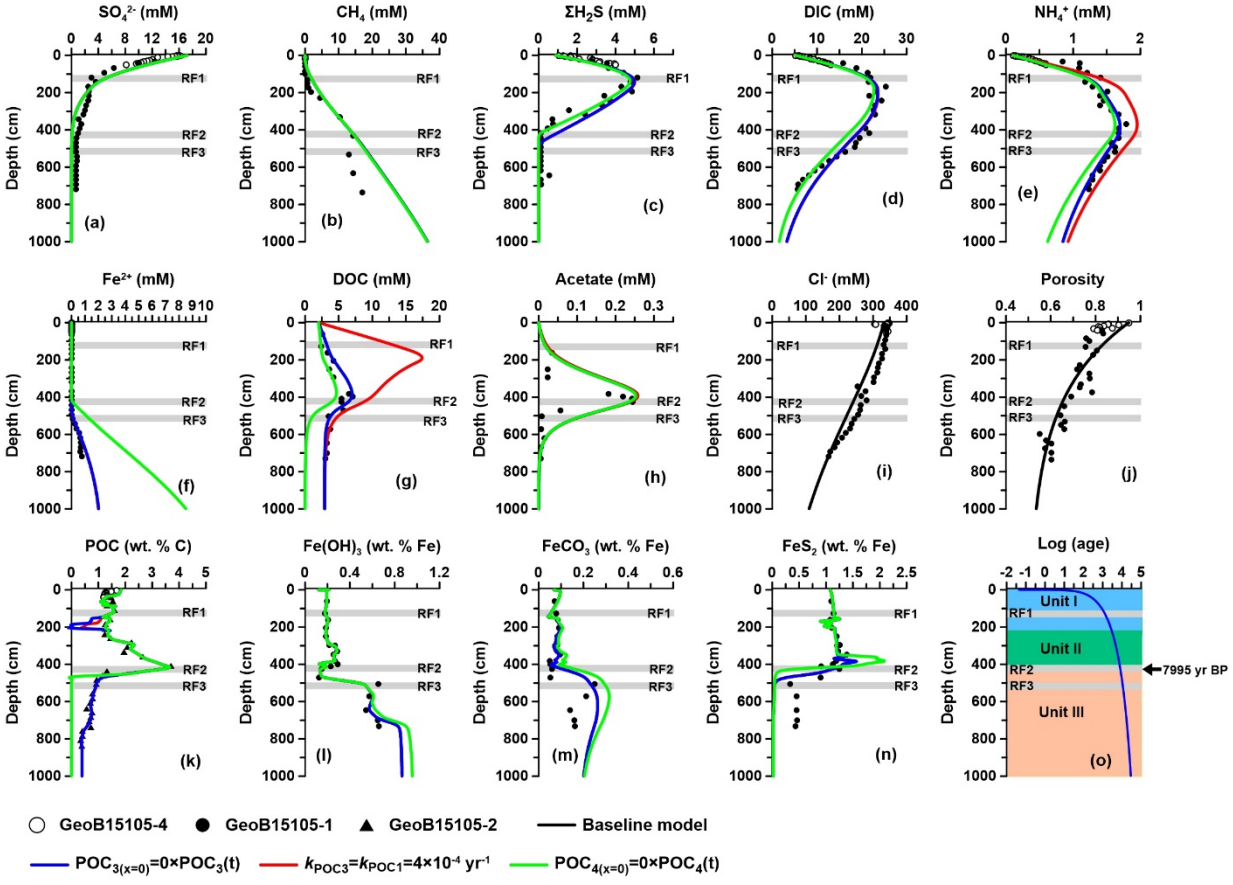

Fig. S4: Model sensitivity analysis of POC_3 and POC_4 content at the upper boundary at site GeoB15105. Baseline values are shown in black curves and measured data as symbols. The grey bars represent the depths of three reaction fronts. The simulated profiles are extracted from the last simulation year. POC_3 and POC_4 inputs and reactivity were constrained by the measured POC contents and DIC and NH_4^+ concentrations.

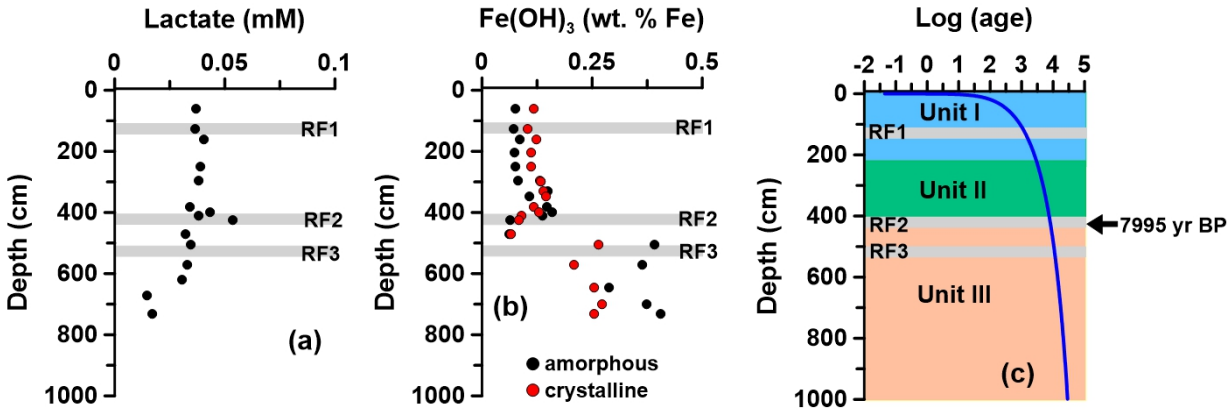

Fig. S5: Measured depth profiles of (a) lactate, (b) amorphous and crystalline iron (oxyhydr)oxides and (c) sedimentology from core GeoB15105-1.

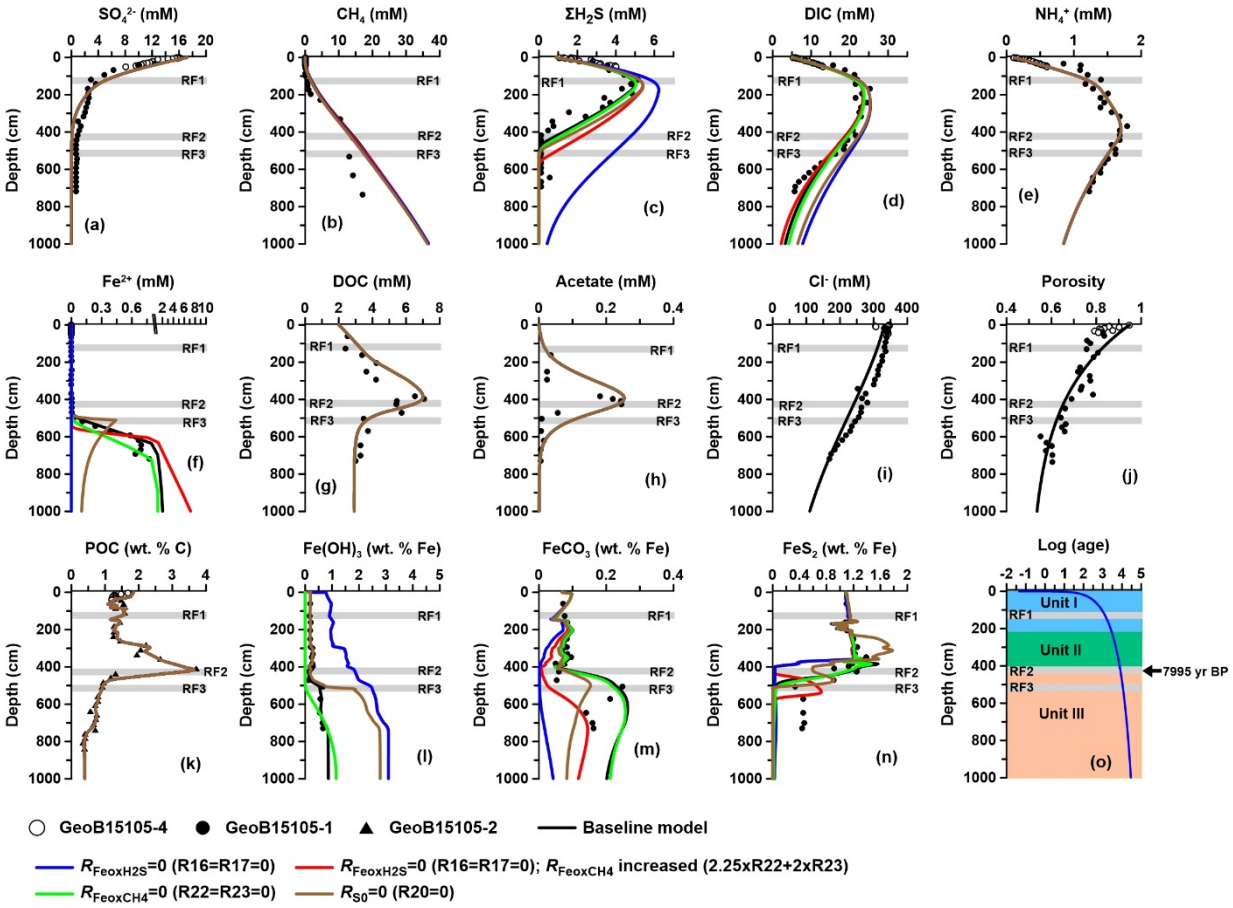

Fig. S6: Model sensitivity analysis of iron oxide reduction coupled with methane oxidation and hydrogen sulphide oxidation at site GeoB15105. Baseline values are shown in black curves and measured data as symbols. The gray bars represent the depths of three reaction fronts. The simulated profiles are extracted from the last simulation year. Results show that Fe^{2+} production is mainly through the cryptic sulfur cycling pathway rather than by coupling with methane oxidation (R22 and R23). Note the break in the axis in (f). The blue and red curve are superimposed in (l).

References

Bahr, A., Lamy, F., Arz, H.W., Major, C., Kwiecien, O. and Wefer, G. (2008) Abrupt changes of temperature and water chemistry in the late Pleistocene and early Holocene Black Sea. Geochemistry, Geophysics, Geosystems 9.

Berner R. A. (1980) Early Diagenesis: A Theoretical Approach. Princeton University Press, Princeton, p. 241.

Bohrmann, G and cruise participants (2011) Report and preliminary results of RV METEOR Cruise M84/2, Istanbul - Istanbul, 26 February - 02 April, 2011. Origin and Distribution of Methane and Methane Hydrates in the Black Sea. Berichte aus dem Fachbereich Geowissenschaften der Universität Bremen, 281. Department of Geosciences, Bremen University. urn:nbn:de:gbv:46-00102252-13

Boudreau B. P. (1997) Diagenetic Models and Their Implementation: Modelling Transport and Reactions in Aquatic Sediments. SpringerVerlag, Berlin, 414p.

Burdige, D.J., Komada, T., Magen, C. and Chanton, J.P. (2016) Modeling studies of dissolved organic matter cycling in Santa Barbara Basin (CA, USA) sediments. Geochimica et Cosmochimica Acta 195, 100-119.

Egger, M., Kraal, P., Jilbert, T., Sulu-Gambari, F., Sapart, C.J., Röckmann, T. and Slomp, C.P. (2016) Anaerobic oxidation of methane alters sediment records of sulfur, iron and phosphorus in the Black Sea. Biogeosciences 13, 5333-5355.

Kwiecien, O., Arz, H.W., Lamy, F., Wulf, S., Bahr, A., Röhl, U. and Haug, G.H. (2008) Estimated Reservoir Ages of the Black Sea since the Last Glacial. 2008, 20.

Lamy, F., Arz, H.W., Bond, G.C., Bahr, A. and Pätzold, J. (2006) Multicentennial-scale hydrological changes in the Black Sea and northern Red Sea during the Holocene and the Arctic/North Atlantic Oscillation. Paleoceanography 21.

Minshull, T.A., Marín-Moreno, H., Betlem, P., Bialas, J., Bünz, S., Burwicz, E., Cameselle, A.L., Cifci, G., Giustiniani, M., Hillman, J.I.T., Hölz, S., Hopper, J.R., Ion, G., León, R., Magalhaes, V., Makovsky, Y., Mata, M.-P., Max, M.D., Nielsen, T., Okay, S., Ostrovsky, I., O'Neill, N., Pinheiro, L.M., Plaza-Faverola, A.A., Rey, D., Roy, S., Schwalenberg, K., Senger, K., Vadakkepuliyambatta, S., Vasilev, A. and Vázquez, J.-T. (2020) Hydrate occurrence in Europe: A review of available evidence. Marine and Petroleum Geology 111, 735-764.

Schulz H. D. (2000) Quantification of early diagenesis: dissolved constituents in marine pore water. In Marine Geochemistry (eds. H. D. Schulz and M. Zabel). Springer-Verlag, Berlin, pp. 85–128.

Soulet, G., Delaygue, G., Vallet-Coulomb, C., Böttcher, M.E., Sonzogni, C., Lericolais, G. and Bard, E. (2010) Glacial hydrologic conditions in the Black Sea reconstructed using geochemical pore water profiles. Earth and Planetary Science Letters 296, 57-66.

Zabel, M. and participants, a. (2012) Biogeochemistry and methane hydrates of the Black Sea; Oceanography of the Mediterranean; Shelf sedimentation and cold water carbonates - Cruise No. M84/1 - February 09 – February 22, 2011 – Valletta (Malta) – Istanbul (Turkey). METEOR-Berichte, M84/1.